Available online at www.sciencedirect.com

ScienceDirect

Journal of Magnesium and Alloys xxx (xxxx) xxx

www.elsevier.com/locate/jma

Full Length Article

Fabrication of ceramic coatings on the biodegradable ZM21 magnesium alloy by PEO coupled EPD followed by laser texturing process

Hariprasad Sampatirao[a], Saikiran Amruthaluru[a], Premchand Chennampalli[a], Rama Krishna Lingamaneni[b], Rameshbabu Nagumothu[a,*]

[a] Department of Metallurgical and Materials Engineering, National Institute of Technology, Tiruchirappalli 620015, India
[b] Centre for Engineered Coatings, International Advanced Research Centre for Powder Metallurgy and New Materials (ARCI), Hyderabad 500005, India

Received 9 May 2020; received in revised form 15 September 2020; accepted 12 October 2020
Available online xxx

Abstract

Zirconia (ZrO_2) incorporated ceramic coatings were fabricated on biodegradable ZM21 Mg alloy by the PEO coupled with EPD process. Subsequently, the sample surface was modified by laser texturing to improve the corrosion resistance, roughness and cell proliferation and growth properties. The corrosion performance of the fabricated samples along with the substrate was studied by electrochemical measurements under simulated body fluid (SBF) environment. The cell direct contact assay was conducted for the substrate and fabricated samples using L-929 mouse fibroblast cells for 24 h. The phase contrast images of cell direct contact assay revealed that fabricated samples exhibited better contact and response with the fibroblast cells, compared to the substrate. The addition of nanoparticles in the PEO process, called PEO coupled EPD process, resulted in attaining a higher thickness and improved corrosion performance of the samples than the PEO coated samples. Among all the samples, laser surface textured PEO, and PEO-EPD coated samples unveiled enhanced corrosion resistance, cell growth, thereby enabling it as a suitable prototype for biodegradable implant applications.

Keywords: ZM21; ZrO_2 nanoparticle; PEO-EPD; Laser texturing; Corrosion resistance; L-929 cells.

1. Introduction

Permanent nondegradable metallic materials like stainless steel, cobalt-chromium, titanium-based alloys have good mechanical properties to be used as load-bearing implants for repair or replacement of damaged bone tissue [1,2]. But the currently used metallic biomaterials result in complications to the host body allied with chronic inflammation and effects of stress shielding [3]. When used for repair, a second surgical intervention may be necessary to remove the implant after the tissues have healed. Also, revision surgery increases the cost and further morbidity to the patient [4]. Moreover, current nondegradable biomaterials have higher density (ρ), elastic modulus (E) and yield strength (YS), i.e. Stainless steel (ρ ~8 gcm^{-3}, E ~200 GPa and Y.S ~310 MPa), cobalt-chromium (ρ ~9 gcm^{-3}, E ~230 GPa and Y.S ~1000 MPa) and titanium (ρ ~4 gcm^{-3}, E ~115 GPa and Y.S ~1117 MPa) based alloys as compared to that of natural bone (ρ ~2 gcm^{-3}, E ~23 GPa and Y.S ~114 MPa) [5-7]. Thus, magnesium and its alloys were highly preferable for biodegradable orthopedic implant applications due to the beneficial combination of mechanical properties, biocompatibility and biodegradability properties [8]. The density (~2 gcm^{-3}), elastic modulus (E ~ 45 GPa), and yield strength (Y.S ~100 MPa) of magnesium (Mg) alloys are similar to those of the bone, which minimizes the stress shielding effects [6]. Mg is nontoxic, and Mg^{2+}ion is one of the most abundant cations in the human body mostly stored in the bone, muscle, and it is involved in the many metabolic reactions and mechanisms [9-11]. Many researchers have worked on magnesium alloys such as AZ31, AM50, AZ80 and AZ91, etc.,

* Corresponding author.
E-mail address: nrb@nitt.edu (R. Nagumothu).

https://doi.org/10.1016/j.jma.2020.10.002

for orthopaedic applications. Unfortunately, these Mg alloys contain aluminium (Al), which is identified to be neurotoxic and causes Alzheimer's disease [12]. Thus, the alloy without aluminium, ZM21 is considered for the present work. The presence of zinc (Zn) improves the corrosion resistance and strength of the material. Also, Zn is one of the essential elements of human body metabolism. Manganese (Mn) improves the yield strength of the alloy. Moreover, ZM21 alloy avoids toxic elements like Al, which is present in most common Mg alloys [13].

Unfortunately, Mg alloys have certain limitations, and Mg dissolves as Mg^{2+} ions, which reacts with water produces the hydrogen bubbles near the implant and creates the hydroxyl groups. H_2 gas causes a toxic effect on the tissues and block the blood vessels [14,15]. However, the main drawback to the application of Mg and its alloys are highly susceptible to corrosion in the biological environment and degrade earlier than the actual period taken for bone healing [16, 17]. Thus, appropriate surface modification techniques are required to reduce the degradation rate of the implant material. Various surface coating techniques are available such as CVD, PVD, thermal spraying, sol-gel, and plasma electrolytic oxidation (PEO) [18,19]. Among these techniques, PEO is a relatively unique technique used to develop a ceramic coating on the light metals (Mg, Al, Zr, Ti) and its alloys to improve wear, corrosion resistance, biocompatibility, and biodegradation rate. Also, the PEO technique is an environmentally friendly process that produces coatings with strong bonding to the substrate [20, 21].

In recent years, many other researchers have investigated the PEO coupled with electrophoretic deposition (EPD) technique to fabricate ceramic composite coatings. PEO coatings fabricated with stable oxide particles, such as CeO_2, TiO_2, Ta_2O_5, ZrO_2, ZnO and Al_2O_3 addition reduced the porosity, degradation rate, increased the scratch resistance, and enhanced corrosion resistance [19,22]. Zirconia (ZrO_2) is commonly used for dental and orthopedic applications due to higher fracture toughness, nontoxicity, bioinertness, and good biocompatibility when compared to other oxides [23]. Thus, in the present study, we choose to incorporate ZrO_2 nanoparticle into a magnesium oxide coating layer by the PEO-EPD process. But the appropriate surface roughness of implant material is essential to favor the process of rapid bone formation for osseointegration [24]. Therefore, laser texturing surface modification technique was used to produce well defined micro-grooves on implant materials to increase the roughness as well as improve the corrosion resistance [25]. Many other researchers reported the main advantage of the laser process i.e., maneuverable surface topography, by varying the laser process parameters such as power, spacing, diameter, and energy density [26,27]. Fiber optical laser is one of the advanced techniques used to produce laser textured surfaces for tribological and biomedical applications. Fiber optical laser is a highly reliable, accurate, and low operating cost laser [28].

However, there is no systematic study on the effect of laser texturing on the physicochemical and electrochemical properties of the PEO and PEO-EPD coatings. In the present study, 4 samples were fabricated on the ZM21 alloy by PEO, PEO-EPD, and the laser texturing of PEO and PEO-EPD. Present work aims to fabricate less porous and corrosion-resistant ceramic composite coating on a ZM21 alloy by incorporating ZrO_2 nanoparticle into the PEO coating by PEO-EPD process followed by a laser texturing process. The PEO coated sample is designated by P, and a composite sample fabricated by combining both the PEO and EPD processes is indicated by PZ, whereas the laser-textured PEO sample is represented by PL and the laser textured PEO-EPD coated sample is indicated by PZL. The wettability, corrosion properties and cell growth of the fabricated samples were compared with the substrate (S).

Table 1
Chemical composition of the ZM21 magnesium alloy.

Element (wt%)	Zn K	Mn K	Si K	Fe K	Ni K	Mg K
ZM21	1.89	0.96	0.31	0.15	0.12	96.57

2. Experimental procedure

2.1. Sample preparation

The ZM21 magnesium alloy (hot rolled plates) obtained from the Defence Research and Development Laboratory (DRDL), Hyderabad, India was used as the substrate in the current study. The chemical composition of the ZM21 alloy used in this study is depicted in Table 1. For the present study, the ZM21 magnesium alloy coupon with dimensions of $19 \times 14 \times 4\,mm^3$ was used as a substrate (S). For the PEO and PEO-EPD coatings, Coupons were mechanically polished, and subsequently, coupons were ultrasonically cleaned with acetone for 4 min and then rinsed with distilled water for 2 min to make the surface free from contaminants and dried in the air before PEO and PEO-EPD coating.

2.2. PEO and PEO-EPD coating fabrication

PEO and PEO-EPD coatings fabricated using a pulsed DC power supply unit (Milman Thin Films Private Limited, Pune, India) with a maximum output voltage of 1000 V and a maximum current of 20 A. The stainless steel bowl containing the electrolyte acts as a cathode, whereas the ZM21 sample acts as an anode. For the PEO coating, an electrolyte comprising of 7 g $Na_2SiO_3 \cdot 9H_2O$ and 3 g KOH in 1 L distilled water was used and it is considered as a base electrolyte solution. For the PEO-EPD composite coating, 4 g monoclinic ZrO_2 (m-ZrO_2) with an average particle size of 45 nm was added into the base electrolyte solution. The aqueous suspension was sonicated using an ultrasonic vibrator for 40 min to ensure particle dispersion. The PEO and PEO-EPD coatings were fabricated at a current density of $160\,mA/cm^2$ corresponding to a current of 1.3 A over a process duration of 10 min. The duty cycle of 20% and a frequency of 1000 Hz were selected for the PEO and PEO-EPD processes. The electrolyte composition, pH, conductivity, breakdown, and final voltage (V_b and V_f)

Table 2
The identification codes for the PEO and PEO-EPD coated samples with their respective electrolyte composition, pH, conductivity and the characteristic voltages.

Sl. no	*Sample code*	*Process*	*Electrolyte composition*	pH	K (mS/cm)	V_b (±2 V)	V_f (±2 V)	*Process time* (min)
1	P	PEO	7 g/l Na_2SiO_3•$9H_2O$ + 3 g/l KOH	12.35	17.95	319	590	10
2	PZ	PEO-EPD	7 g/l Na_2SiO_3•$9H_2O$ + 3 g/l KOH + 4 g/l ZrO_2	12.09	16.33	345	644	10

values are reported in Table 2. Finally, coated samples were ultrasonically cleaned and dried at room temperature before the laser texturing process.

2.3. Fabrication of laser textured samples

The laser textured samples were carried out by optical fiber laser (MLS-F60, Meera laser solutions, Chennai, India). The laser source is an optical fiber doped with rare earth element Ytterbium (Yb^{3+}) with a maximum output power of 60 W equipped with a laser beam wavelength of 1064 nm, frequency of 20 kHz and traversing speed of 150 mm/s. The optical fiber laser source at a constant power of 21 W (i.e. 31% of 60 W), the energy density of 53.42 J/cm^2, beam diameter of 35 μm, energy per pulse of 10.5×10^{-4} J, pulse duration of 50 μs, the focal length of 193 mm and line spacing of 235 μm and were used to carry out the laser surface modification of the PEO and PEO-EPD samples. For comparison purposes, the same laser process parameters were used for both PEO and PEO-EPD coated samples. The PEO and PEO-EPD fabricated samples along with their identification codes, referred to as P and PZ are shown in Table 2.

2.4. Characterization of the samples

The phases present in the substrate and fabricated samples were analysed by the XRD technique using ultima-IV, (Rigaku, Japan) rigged with a Cu target. The XRD analysis was performed at a scan speed of 1°/ min over a scan range (2θ) of 20°−85° with a step size of 0.02°. Phase identification of the coatings done with standard JCPDS cards. The morphology and compositional studies of the fabricated samples were analysed by field emission scanning electron microscope (FESEM, GeminiSEM 300, Carl Zeiss, Germany) equipped with an energy dispersive spectroscopy (EDAX, AMETEK, USA). The 3D-optical and depth profile of the samples and the average surface roughness (R_a) were studied by using a scanning white light interferometer (Talysurf CCI, Taylor-Hobson, UK). By using a 20X objective lens, the surface roughness measurements of the samples were carried out over an area of 0.8×0.8 mm^2 in five different places, and the roughness value was reported.

Scratch testing was used to determine the adhesion strength of the coatings to the substrate. The scratch tester has a Rockwell C Diamond stylus (Revtest, CSM Instruments, Switzerland). The radius of the stylus is 200 μm and the scratch test was performed with a progressive load ranging from 1 to 40 N. The stylus is moved across the surface of fabricated samples with a traversal speed of 2.5 mm/min over a scratch length of 5 mm. The hydrophilicity and hydrophobicity nature of the samples was studied by DSA100 (KRUSS, Germany) contact angle goniometer. Double distilled water was used as a contacting solvent and the volume of the droplet was fixed as 3 μL.

2.5. Electrochemical test

Electrochemical corrosion studies were conducted in a 7.4 pH SBF environment at ambient temperature. SBF was prepared by Kokubo's standard procedure [29], and 250 ml of the SBF medium was used for the corrosion study. Potentiodynamic polarization (PDP) and the electrochemical impedance spectroscopy (EIS) plots were obtained using a potentiostat (Gill ACM instruments, UK) to evaluating corrosion properties of the substrate (S) and fabricated samples (P, PL, PZ and PZL). The evaluation of corrosion resistance for the samples (working electrode) was carried out in a 3-electrode cell setup against the platinum foil (counter electrode), by considering the saturated calomel electrode (SCE) as a reference electrode. PDP test was conducted by polarizing the samples between −300 mV to + 300 mV with reference to the open circuit potential (OCP) at a rate of 10 mV/min as per the ASTM standard G 59–97. The corrosion current density (i_{corr}) was evaluated by tafel analysis with reference to OCP. The AC signal of the amplitude of ±10 mV with frequency ranging between 1E-2 Hz to 10E5 Hz was used to examine the frequency response of the fabricated samples along with the bare substrate by EIS studies. The EIS experimental data were analysed by the equivalent circuit modeling and curve fitting of experimental data by using the Z-view software.

2.6. Direct contact assay

The direct contact assay was performed for the substrate (S), PEO, PEO-EPD, and laser textured samples (P, PZ, PL and PZL) using standard L-929 mouse fibroblast cell line (Biogenix Research Centre, Trivandrum, India). The cytotoxicity of the substrate (S), P, PZ, PL and PZL samples was determined by direct contact assay. Prior to the direct contact assay, all the samples were sterilized with ultraviolet (UV) irradiation for 1 h and then directly taken for analysis. L-929 mouse fibroblast cells 100 μL (1×10^5 cells/sample) were

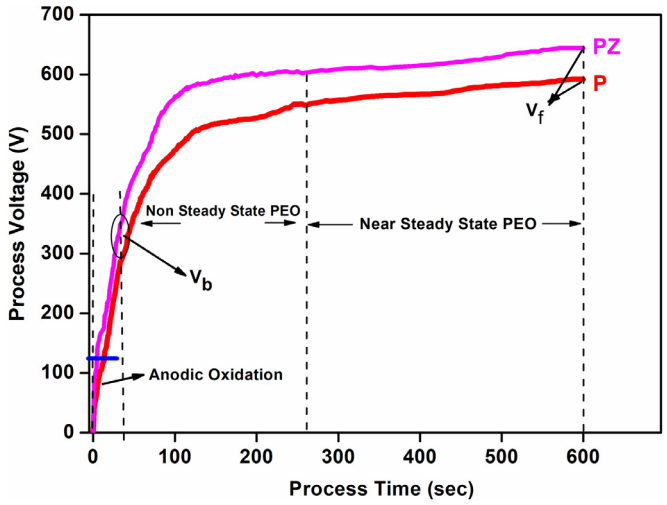

Fig. 1. *V–T* plots during the PEO and PEO-EPD process.

seeded on the tissue culture plate and allowed to grow for 24 h. Fabricated samples along with the substrate were then placed in the tissue culture plate and were allowed to proliferate for 1 day in a 5% CO_2 incubator. Morphological changes of the 24 h incubated L-929 fibroblast cells over the samples along with the cells grown on the control (without material) were evaluated by phase-contrast microscopy.

3. Results and discussion

3.1. PEO and PEO-EPD process

During the PEO and PEO-EPD processes, the variation of voltage to time is recorded, and the voltage vs time graphs was plotted as shown in Fig. 1. The mechanism of the PEO coating can be categorized into 3 regimes, namely anodization, dynamic PEO, and steady-state PEO [30]. During the initial stage of the process, i.e., anodization, the formation of a thin passive oxide layer happens without any visible sparking. The second stage starts at breakdown voltage, corresponding to the first inflection point in the voltage vs time graph. During the second stage, a vast number of fine white sparks are observed to rapidly scan over the surface of the specimen. During the final stage, sparking is established over the anodic surface, and the voltage becomes relatively stable. The second inflection point is known as the critical voltage at which the white sparks become more intense and turns orange in color. The PEO and PEO-EPD coatings' electrolyte system composition, pH, and conductivity of the electrolyte, as reported in Table 2. During the PEO and PEO-EPD processes, the breakdown voltage (V_b) was noted at the micro discharges start to appear on the substrate, and final voltage (V_f) values were recorded at the end of the process, 10 min, as shown in Table 2. The V_b values corresponding to the P and PZ samples are 319 V and 345 V, respectively. On the other hand, the conductivity of the electrolyte used for P and PZ are 17.95 mS/cm and 16.33 mS/cm, as reported in Table 2. The conductivity of the electrolyte was decreased due to the addition of ZrO_2 nanoparticle suspension to the base electrolyte. The ZrO_2 nanoparticle addition increased both V_b and V_f corroborating with the decrease in conductivity of the electrolyte as reported in Table 2. It agrees with the Ikonopisov's theoretical model, which relates the breakdown voltage and conductivity of the electrolyte by the following equation [31]:

$$V_b = A_b + B_b \log\left(\frac{1}{k}\right) \quad (1)$$

where V_b is the breakdown voltage, k is the conductivity, A_b and B_b are constant values for substrate and electrolyte composition, respectively.

3.2. Phase composition of the samples

The XRD patterns of the fabricated samples P, PL, PZ, and PZL are shown in Fig. 2(a). All the samples contain MgO and Mg_2SiO_4 (JCPDS No: 85-1364 and 78-0430) along with the substrate peaks. In addition to m-ZrO_2 and $Mg_2Zr_5O_{12}$ (JCPDS No: 41-0185 and 37-1448) phase was observed for PZ and PZL samples as indicated by black color circles as depicted in Fig. 2(b). The general reactions of oxidation of Mg and its alloys during the PEO and PEO-EPD processes are as follows [3,32].

$$Mg^{2+} + 2(OH^-) \rightarrow Mg(OH)_2 \rightarrow MgO + H_2O \quad (2)$$

$$2Mg^{2+} + SiO_3^{2-} + 2(OH^-) \rightarrow Mg_2SiO_4 + H_2O \quad (3)$$

$$2Mg^{2+} + 5ZrO_2 + 4(OH^-) \rightarrow Mg_2Zr_5O_{12} + 2(H_2O) \quad (4)$$

In PZ and PZL samples, ZrO_2 nanoparticle incorporation by PEO-EPD process formed m-ZrO_2 and $Mg_2Zr_5O_{12}$ phases in the coatings along with the MgO and Mg_2SiO_4 phases. Similar observations were also reported by Lee et al. [33] and Arrabal et al. [34]. This indicates the partially reactive incorporation of m-ZrO_2 nanoparticles in the coatings. As compared to P and PZ samples, the intensity of the MgO and Mg_2SiO_4 peaks found to be increased in PL and PZL samples, as shown in Fig. 2(b). Re-melting of the oxide layers during the laser texturing process leads to an increase in the local temperature, which in turn leads to an increase in the form of crystalline MgO and Mg_2SiO_4 phase.

3.3. Surface morphology and composition

Fig. 3(a)–(d) shows FESEM surface micrographs and EDS spectra of the samples P, PL, PZ and PZL, respectively, it can be observed that all samples showed different morphologies i.e., porosity, microcracks, rough surface, laser tracks, and grooves. From Fig. 3(a), sample P exhibited a crater-like microstructure with open pores and microcracks on the surface, which are common characteristic features of the coating fabricated by the PEO process. Open pores occurred due to

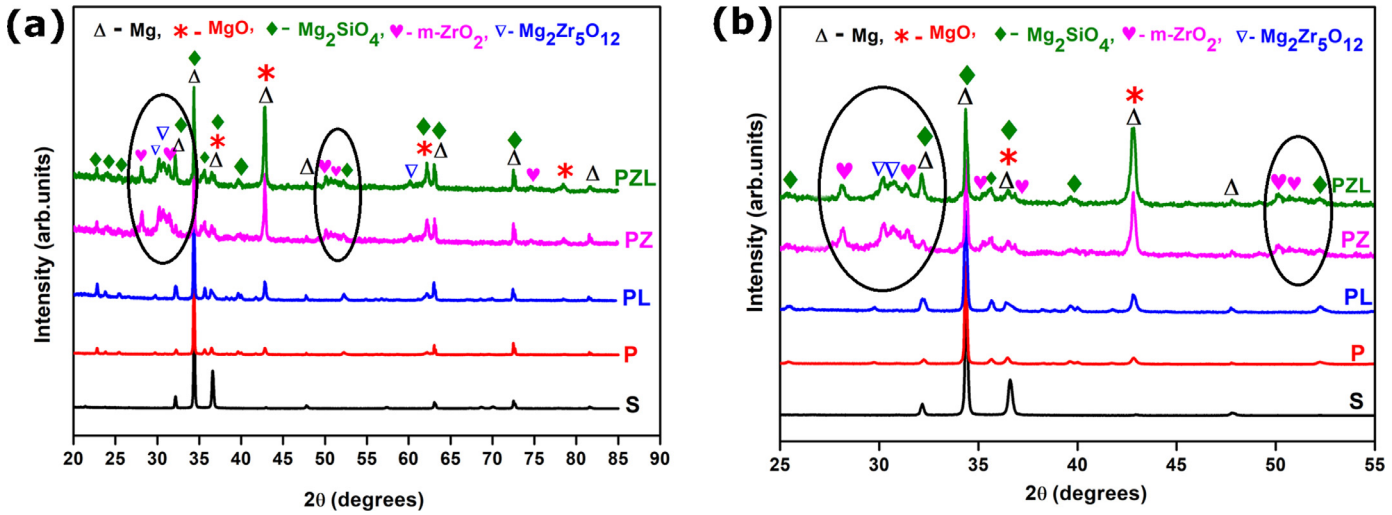

Fig. 2. XRD patterns (a) 20°−85° (b) 25°−55° for the substrate (S), P, PL, PZ and PZL samples.

the gas evolution through the discharge channels. The microcracks were generated due to the thermal stress experienced during coating formation [3]. As shown in Fig. 3(c), PZ sample exhibited a dense coating with closed pore structure than the sample P, which can be attributed to the m-ZrO_2 nanoparticle incorporation into the oxide layer formed by the plasma discharges. The negatively charged m-ZrO_2 nanoparticles can be attracted into the plasma discharge channels and incorporated into the oxide coatings formed by the plasma discharges. Many other researchers reported that the incorporation of nanoparticles has a significant effect on the properties of PEO coatings, such as the reduction in porosity and improvement in hardness [23, 33]. On the other hand, the surface morphology of laser-treated samples PL and PZL are comparable, and these surfaces appear to be completely different than the samples P and PZ. As compared to P and PZ samples, the pores and cracks are covered by the molten oxide layer in PL and PZL samples, as shown in Fig. 3(b) and (d). The surface morphology of PL and PZL samples exhibit the molten oxide layer formation along with laser tracks and grooves over the sample surface, and it was attributed to the penetration of the laser beam on the sample surface during the laser texturing process. Due to the laser irradiation, the oxide layer melts and forms small spherical and granular shapes spreaded over the sample surfaces, and grooves were formed at the intersecting point of the vertical and horizontal laser tracks. The distance between adjacent laser tracks (edge to edge) and the width of the laser track are $234.7 \pm 2.7\,\mu m$ and $35.4 \pm 1.4\,\mu m$, respectively obtained by averaging 10 measurements from the FESEM images. On the other hand, the sample PL showed slightly higher laser track depth than the PZL sample, due to the bigger open pore structure of sample P as compared to the sample PZ exhibiting dense coating with closed pore morphology.

The surface EDS spectra of the P, PL, PZ and PZL samples are shown in Fig. 3. According to the EDS analysis, all the samples exhibited the characteristic peaks corresponding to O, Mg, Zn, Mn, Na, Si and K. In addition to these elements, Zr is present in PZ and PZL samples. From Fig. 3, the higher intensity of peaks was observed for Mg, Si, O and Zr elements attributed to the fabricated samples with MgO, Mg_2SiO_4, m-ZrO_2 and $Mg_2Zr_5O_{12}$ phases observed in the XRD phase analysis shown in Fig. 2. The elemental composition of the samples was reported in Table 3. Among all the samples, PL and PZL samples exhibited higher atomic percentage of oxygen, attributed to the irradiation of the laser beam, the surface quickly melted, solidified and became oxidized [26].

3.4. Cross-sectional microstructures and EDS analysis

The coating thickness of the P, PL, PZ and PZL samples was evaluated by FESEM cross-sectional microstructures, as shown in Fig. 4. The average coating thickness values are reported in Table 4. The average coating thickness of the P, PL, PZ and PZL samples are $33.5 \pm 1\,\mu m$, $33.2 \pm 1\,\mu m$, $48.5 \pm 1\,\mu m$ and $48.9 \pm 1\,\mu m$, respectively. From Fig. 4, the thick and dense coating was observed for the PEO-EPD sample (PZ) than that of the PEO sample (P), which can be due to the m-ZrO_2 nanoparticle addition in the respective electrolyte. On the other hand, the PL and PZL samples exhibited laser affected regions (i.e., grooves) which are marked with the red color rectangular box, as shown in Fig. 4(b) and (c). These grooves were formed at the intersecting points of the vertical and horizontal laser tracks, as shown in Fig. 3. The elemental maps for the P, PL, PZ and PZL cross-sections are shown in Fig. 5. The elemental mapping confirmed the presence of the Mg, O and Si elements in the P, PL, PZ and PZL samples, and the distribution of the Zr element was confirmed by the elemental maps of the PZ and PZL samples, shown in Fig. 5.

3.5. Scratch resistance of the samples

The adhesion between the substrate and coating was evaluated using a scratch tester by producing a scratch on the

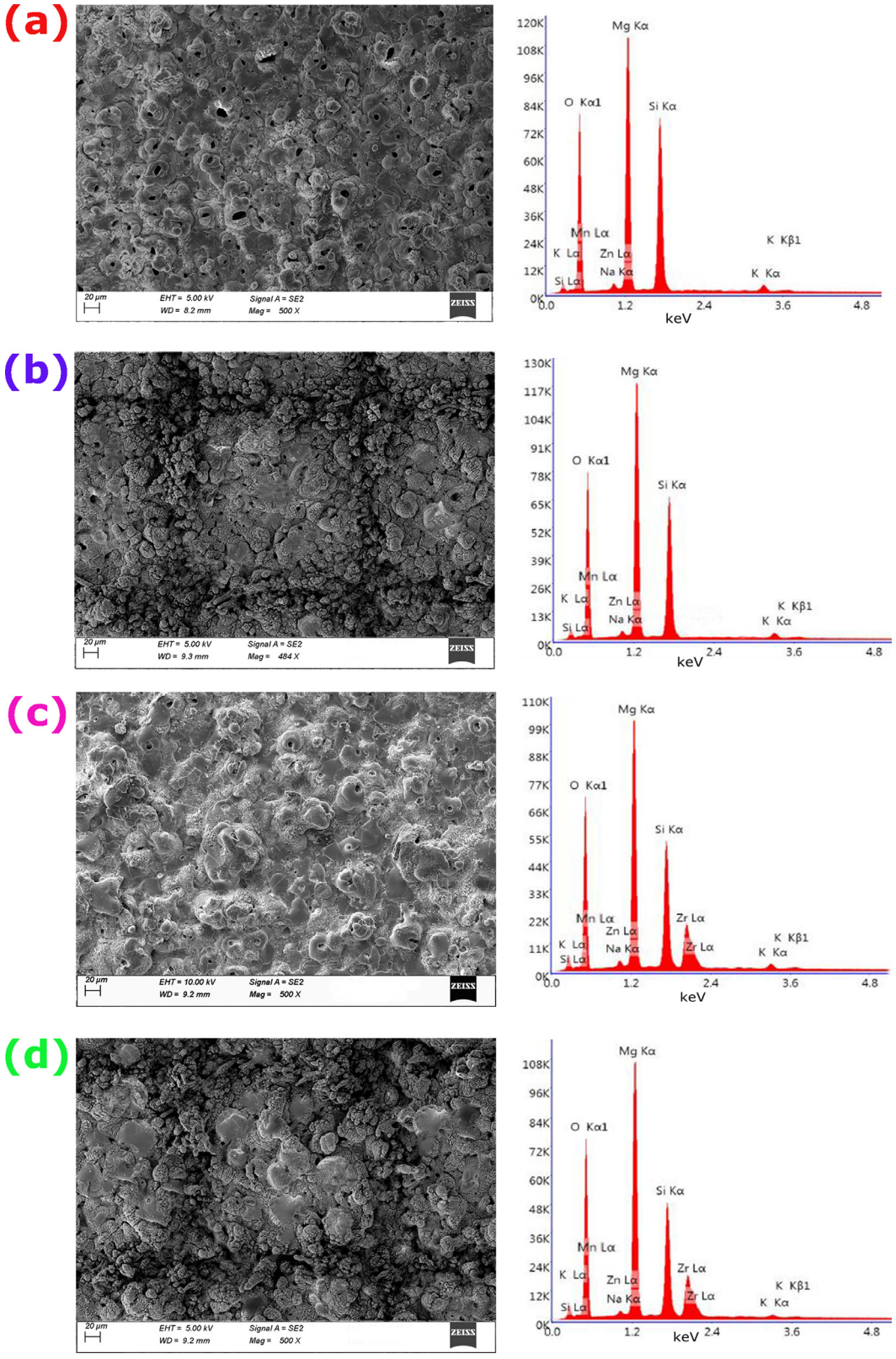

Fig. 3. FESEM surface morphology and EDS spectra of the P, PL, PZ and PZL samples.

Table 3
Elemental composition of the P, PL, PZ and PZL samples.

Sample code	*Element* (at%)							
	O K	Mg K	Zn K	Mn K	Na K	Si K	K	Zr L
P	52.09	32.47	0.23	0.16	0.71	13.68	0.66	–
PL	53.72	31.85	0.22	0.23	0.76	12.65	0.57	–
PZ	55.76	27.07	0.20	0.19	0.83	12.18	0.52	3.25
PZL	56.90	27.94	0.23	0.20	0.75	12.32	0.54	3.12

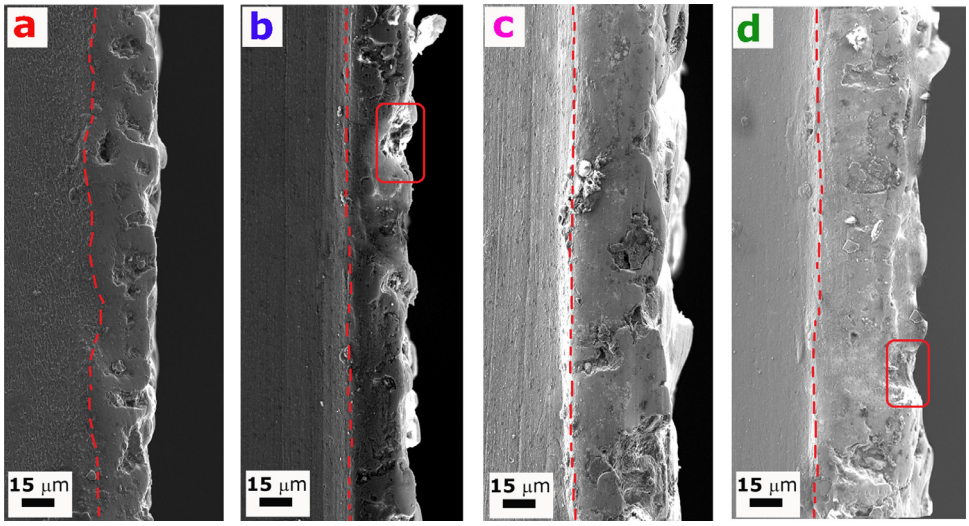

Fig. 4. FESEM cross-sectional microstructures of the P, PL, PZ and PZL samples.

Table 4
The coating thickness (t), critical load (L_c) and corresponding friction forces (F_t) and contact angle (θ) values of substrate (S), P, PL, PZ and PZL samples.

Sample code	t (±1 μm)	L_c (N)	F_t (N)	θ (°)
S	–	–	–	58
P	33.5	28.10	11.87	6.1
PL	33.2	28.16	11.39	7.5
PZ	48.5	33.28	14.02	9.8
PZL	48.9	33.16	14.13	12.3

fabricated sample surfaces. The load at which delamination of the coating takes place over the scratch track is defined as the critical load (L_c). During the scratch test, panoramic view of the scratch track of P, PL, PZ and PZL samples obtained using an optical microscope. The scratch track images along with the frictional force vs load graphs of the samples are shown in Fig. 6. The L_c and frictional force values corresponding to the delamination (F_t) of the samples are reported in Table 4. As compared to the P and PL samples with 28.10 N and 28.16 N, the PZ and PZL samples showed higher critical loads 33.28 N and 33.16 N, respectively. The L_c value depends on thickness, phase composition, hardness, and compactness of the coatings [35]. From the load vs friction force curves depicted in Fig. 6, it can be noted that the friction force linearly increased with an increase in load for samples P and PZ. Whereas, the load vs friction force curves show small oscillations for PL and PZL samples due to the laser tracks on the sample surface. Among all the samples, PZ and PZL samples exhibited higher resistance against the stylus movement.

3.6. Wettability of the samples

Wettability of the substrate (S), P, PL, PZ and PZL samples was estimated by the contact angle measurement. Fig. 7 shows the water droplet photographs of the samples S, P, PL, PZ and PZL. The contact angles of the substrate (S), P, PL, PZ and PZL are 58°, 6.1°, 7.5°, 9.8° and 12.3°, respectively, and are presented in Table 4. The wettability of the coated sample relies on the chemical composition and morphology of the surface [36]. From Table 4, it can be noted that the contact angles for all samples are less than 13° indicating its good hydrophilicity. Also, Li et al. [26] studied that laser spacing between the two laser tracks varying from 50 μm to 300 μm and reported that the contact angle decreased with increasing the laser track spacing. All the coated samples in this study exhibited good wettability as compared to the substrate, which indicates that the coated samples fabricated in the present study are expected to induce favorable cell attachment and cellular interactions [37] on their surfaces.

3.7. Electrochemical test

3.7.1. OCP measurement

Fig. 8 shows the OCP curves of the P, PL, PZ and PZL samples along with the substrate for 4 h. The OCP values

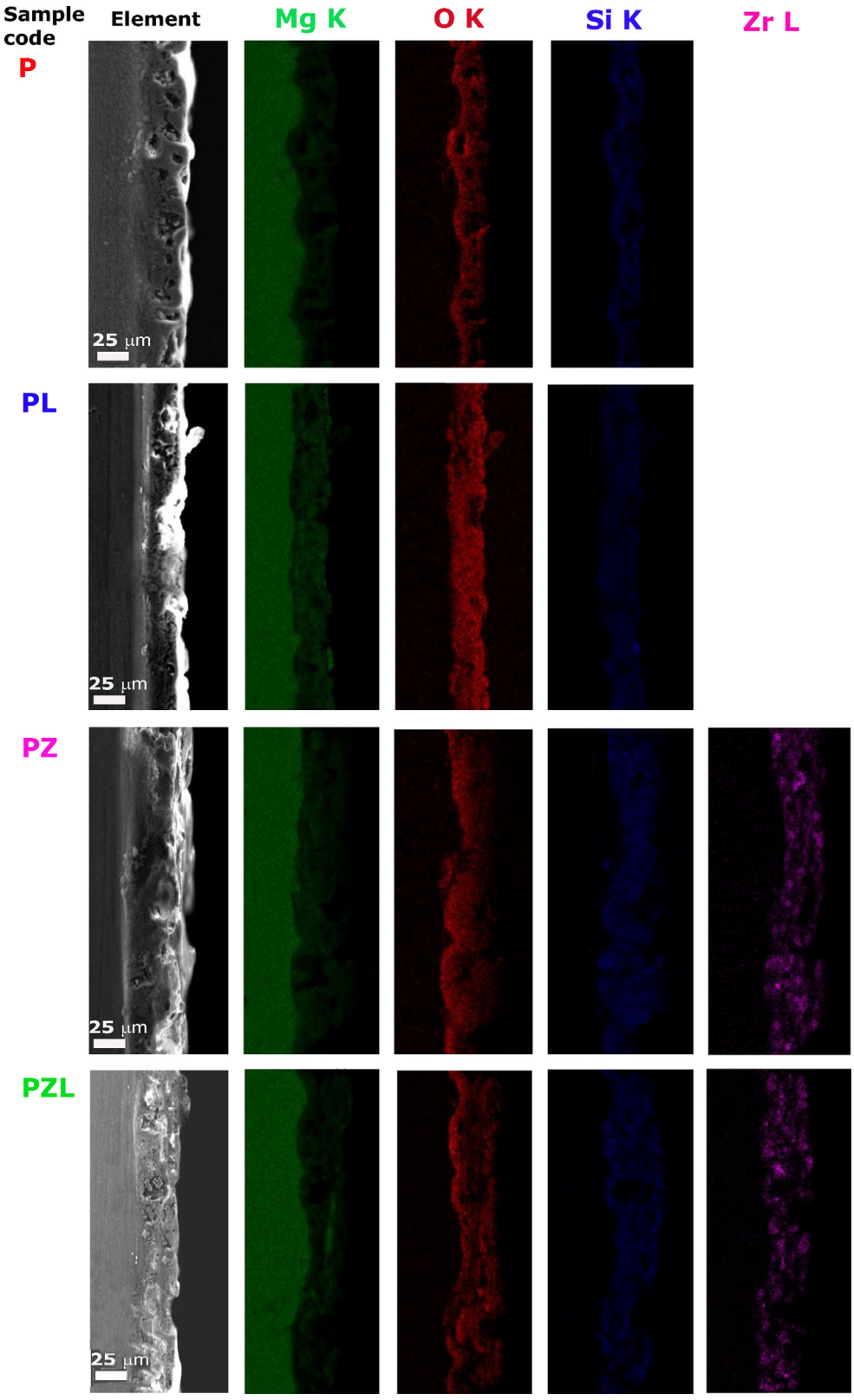

Fig. 5. FESEM cross-sectional micrographs and corresponding elemental maps for the P, PL, PZ and PZL samples.

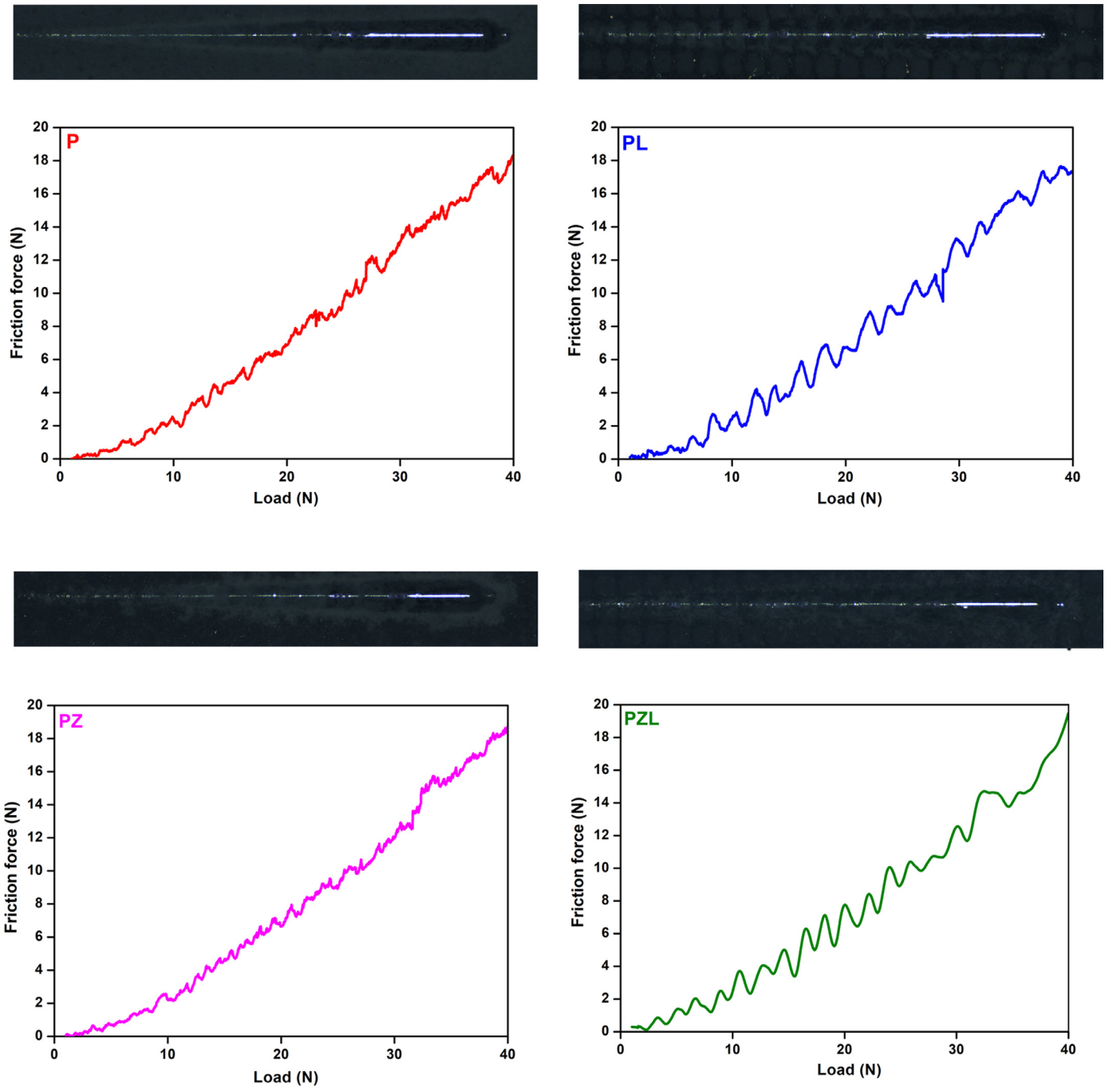

Fig. 6. Panoramic optical micrographs and the corresponding friction force vs load measured during scratch testing of the P, PL, PZ and PZL samples.

Table 5
The PDP results obtained from the Tafel analysis of substrate (S), P, PL, PZ and PZL samples in 7.4 pH SBF medium.

Sample code	E_{OCP} *Vs SCE* (mV)	E_{Corr} *Vs SCE* (mV)	$\lvert\beta_c\rvert$ (mV/decade)	β_a (mV/decade)	i_{corr} (mA/cm^2)
S	−1598	−1603	409	195	0.121
P	−753	−769	281	624	2.04×10^{-4}
PL	−683	−691	540	629	2.36×10^{-5}
PZ	−434	−448	263	278	1.47×10^{-7}
PZL	−359	−364	315	454	1.73×10^{-8}

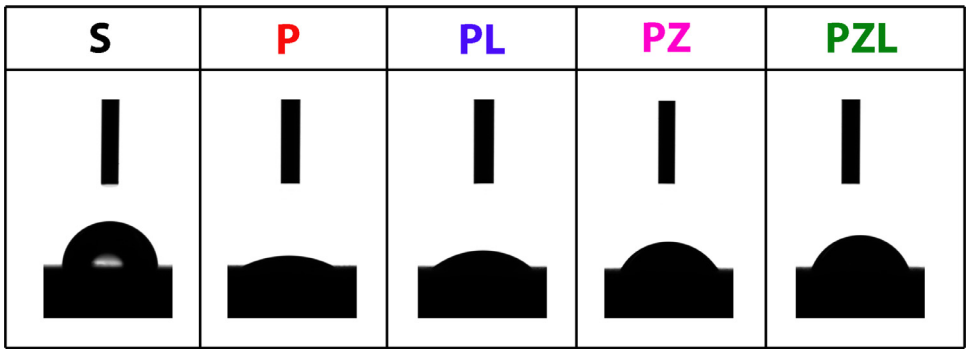

Fig. 7. Water droplet images of the substrate (S), P, PL, PZ and PZL samples.

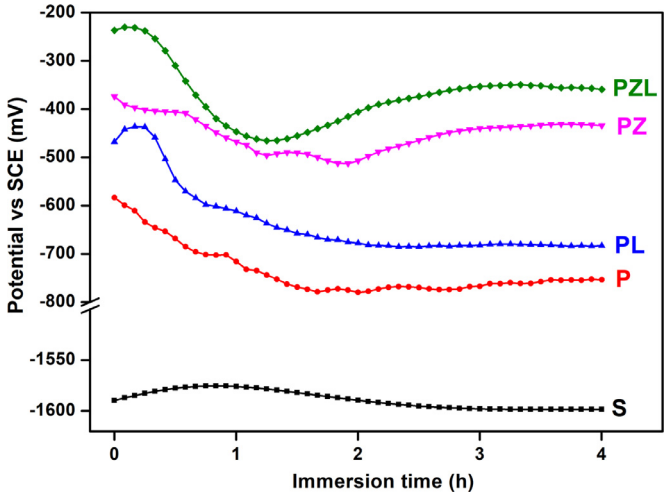

Fig. 8. OCP curves of the substrate (S), P, PL, PZ and PZL samples over an immersion period of 4 h.

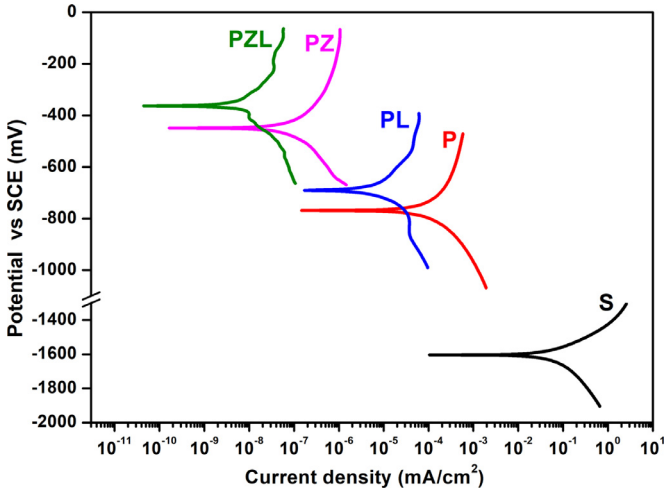

Fig. 9. Potentiodynamic polarization curves of the samples substrate (S), P, PL, PZ and PZL samples.

are listed in Table 5. From Table 5, it is observed that OCP values for the P, PL, PZ and PZL samples were higher than the substrate, which indicates better corrosion protection offered by the surface-modified samples compared to the substrate. From Fig. 8, it is observed that the OCP of P sample decreased from −583.4 mV to −778.9 mV over the exposer time of 1 h 40 min and similarly, the PZ sample decreased from −373.7 mV to −507.1 mV during the initial 2 h and then maintained stable OCP value up to 4 h. In the case of the PL sample, the OCP increased from −467.6 mV to −437.1 mV during the initial 15 min and then decreased from −437.1 mV to −675.2 mV over an immersion time of 1 h 50 min and then almost maintained stable OCP value up to 4 h. On the other hand, the OCP of the PZL sample decreased from −236.6 mV to −465 mV over an exposure time of 1 h 20 min and then gradually increased and maintained a stable value. The trend of decrease or increase during the initial stage of OCP of the fabricated samples can be ascribed to the changes in the cathodic and anodic reactions around the coating/solution interface. PZ samples showed higher stable potential than that of the P sample, which is attributed to the higher thickness and pore-free morphology. On the other hand, laser surface modified of PEO, PEO-EPD coated samples (PL and PZL) exhibited higher stable potential than P and PZ samples. It indicates that the laser texturing resulted in the significant improvement in the thermodynamic stability, due to the closure of the pores and cracks by the molten oxide layer during laser treatment in the PL and PZL samples. OCP values of the fabricated samples were found to be stabilized over a period of 4 h indicating the establishment of corrosion equilibrium condition as shown in Fig. 8. Among all the samples, PZ and PZL samples exhibited a higher resistive behavior, which is due to the occurrence of pore-free surface morphology, higher thickness, and enhanced contact angle.

3.7.2. PDP studies

The corrosion resistance of the PEO, PEO-EPD, and laser textured samples along with the substrate (S) was estimated by the PDP study. The PDP test results are shown in Fig. 9. The polarisation test parameters E_{corr}, i_{corr}, β_c and β_a values of the substrate (S), P, PL, PZ and PZL samples are presented in Table 5. The E_{corr} values of the PEO, PEO-EPD, and laser textured samples P, PZ, PL and PZL, respectively, showed more positive values than the substrate (S), as reported in Table 5. On the other hand, the i_{corr} values of substrate (S), P, PL, PZ and PZL samples

Table 6
Various electrical parameter values obtained after equivalent circuit fitting from the EIS data for substrate (S) and P, PL, PZ and PZL samples.

Sample code	R_s (Ω-cm^2)	CPE_{op}-T (Ω^{-1} cm^{-2})	CPE_{op}-P	R_{op} (Ω-cm^2)	CPE_b-T/CPE_{ib}-T (Ω^{-1} cm^{-2})	CPE_b-P/CPE_{ib}-P	R_b/ R_{ib} (Ω-cm^2)	W_o-R (Ω-cm^2)	W_o-T (s)	W_o-P	R_L (Ω-cm^2)	L (H)	X^2
S	43	–	–	–	6.94×10^{-5}	0.68	2.46×10^2	–	–	–	1.53×10^{-6}	8.12×10^2	5.8×10^{-3}
P	18	5.24×10^{-7}	0.78	3.42×10^4	4.27×10^{-6}	0.32	1.53×10^7	3.22×10^6	52	0.41	–	–	4.4×10^{-3}
PL	22	3.61×10^{-9}	0.84	1.91×10^5	7.53×10^{-8}	0.26	9.14×10^6	–	–	–	–	9.69×10^6	1.7×10^{-4}
PZ	25	4.18×10^{-8}	0.43	9.43×10^7	1.02×10^{-6}	0.39	7.27×10^9	1.64×10^8	78	0.37	–	–	2.3×10^{-3}
PZL	37	2.22×10^{-10}	0.85	4.95×10^8	1.54×10^{-8}	0.19	5.63×10^9	–	–	–	–	5.54×10^9	$3..4 \times 10^{-3}$

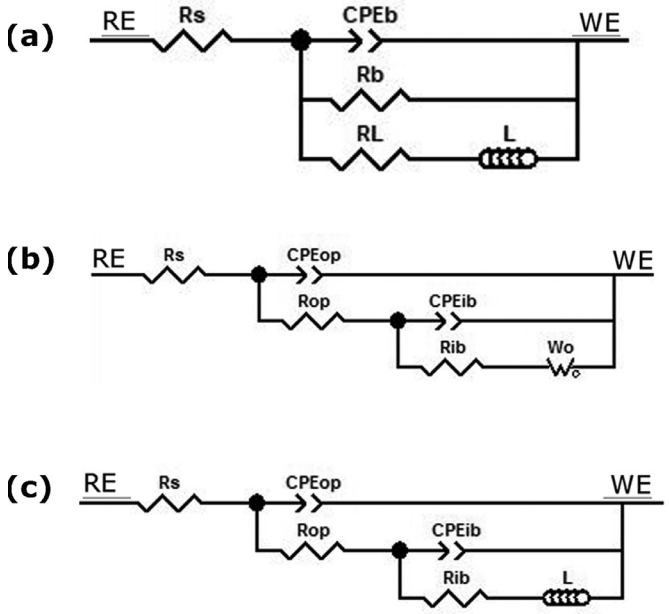

Fig. 10. The equivalent electrical circuits of EIS fitting for (a) the substrate (S), (b) the P and PZ (c) the PL and PZL samples.

are 0.121 mA/cm^2, 2.04×10^{-4} mA/cm^2, 2.36×10^{-5} mA/cm^2, 1.47×10^{-7} mA/cm^2 and 1.73×10^{-8} mA/cm^2, respectively. The samples P, PL, PZ and PZL exhibited much lower i_{corr} than that of the substrate (S). The lower i_{corr} represents slower kinetics in the corrosion process [38]. From the PDP results, the PZ sample exhibited higher corrosion resistance with a lower i_{corr} compared to the P sample, which can be ascribed to its pore-free surface morphology with a dense and thick coating due to incorporation of zirconia nanoparticles. In the case of the P sample, the micropores that occurred during the PEO process leads to the influence of decreasing the corrosion resistance and increasing the degradation rate. Compared with the PZ sample, the sample P is having relatively higher roughness and lower contact angle favoring the degradation. The ZrO_2 nanoparticle addition to the PEO electrolyte system, and thereby developing a nanoparticle incorporated composite oxide coating by PEO coupled EPD process with superior corrosion resistance on Cp-Ti is reported elsewhere [23]. The laser textured PEO and PEO-EPD coatings (PL and PZL) exhibited higher corrosion resistance than that of P and PZ samples. The laser textured PEO sample (PL) showed lower current density (i_{corr} =2.36×10^{-5} mA/cm^2) than that of the P sample (i_{corr} =2.04×10^{-4} mA/cm^2), which can be accredited to the covering of a majority of pores and cracks by the molten oxide layer during the laser texturing process. On the other hand, the laser textured PEO-EPD sample PZL, exhibited higher corrosion resistance with lower current density (i_{corr} =1.73×10^{-8} mA/cm^2) than that of the PZ sample (i_{corr} = 1.47×10^{-7} mA/cm^2) due to modified surface morphology and lower wettability. As compared to the laser textured PL, the laser textured PEO-EPD sample PZL showed lower i_{corr}, which can be ascribed to its compact microstructure, higher thickness, enhanced scratch resistance and lower

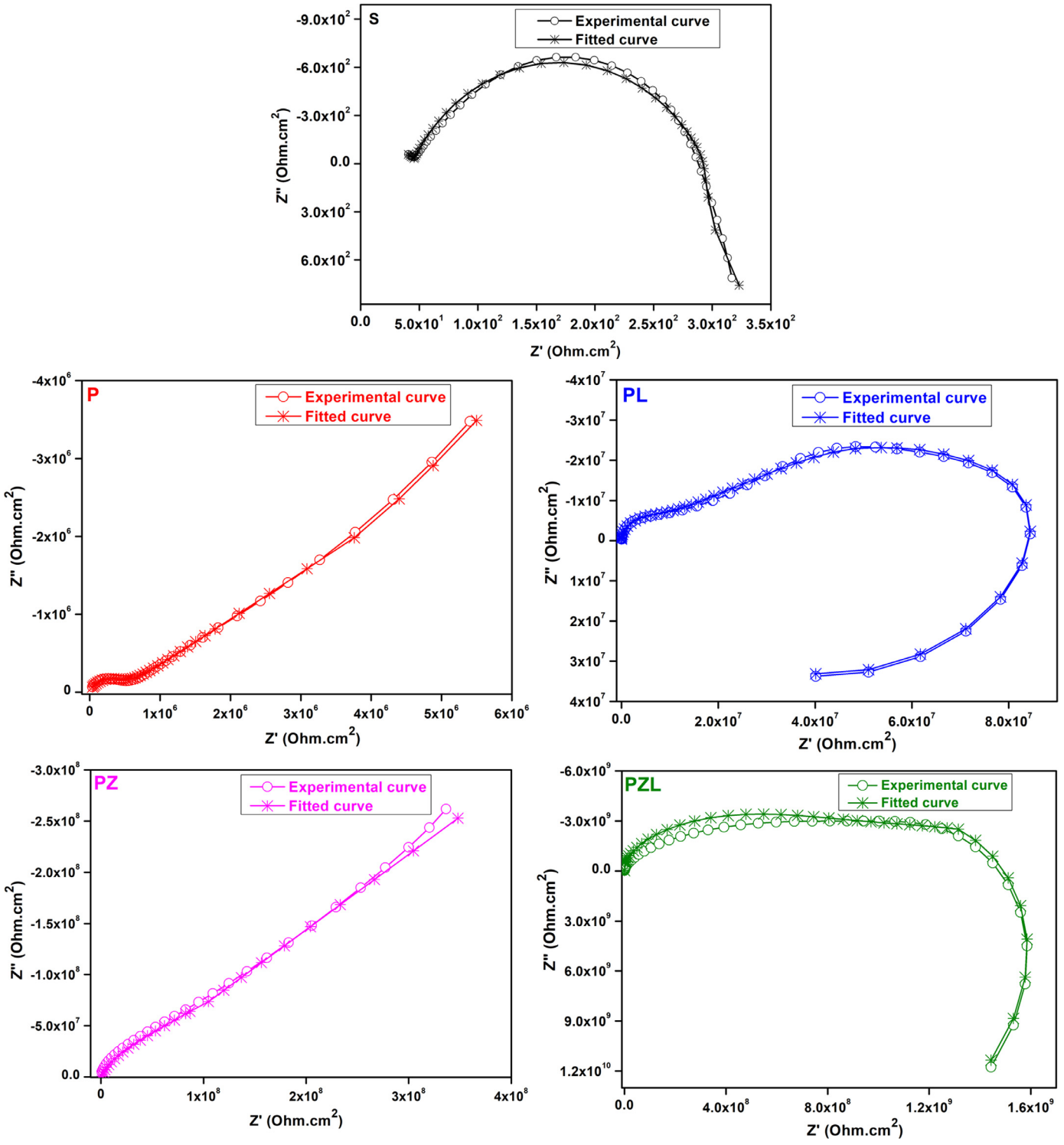

Fig. 11. The Nyquist plots of the samples substrate (S), P, PL, PZ and PZL samples.

wettability. Among all the samples, the PZL sample fabricated by PEO-EPD followed by laser texturing exhibited more positive corrosion potential value and lower i_{corr} value. It can be ascribed to the higher coating thickness along with the compactness of the coating with nearly pore-free morphology, and the presence of small spherical and granular structures as apparent from the surface morphology, as shown in Fig. 3.

3.7.3. EIS studies

EIS test was employed to study the frequency response characteristics of the substrate, PEO, PEO-EPD, and laser textured PEO and PEO-EPD samples. The EIS test results of the samples are presented in Figs. 10–13. Fig. 10 shows the equivalent electrical circuits which best fit to the experimental data. The fitting quality of the samples along with

the substrate was evaluated by Chi-square (χ^2) value, which is in the order of 10^{-3}, describing a good quality of the fit and the values of the electrical parameters attained from the fitted results, are reported in Table 6. The equivalent circuit contained different electrical parameters such as R_s, R_{op}, R_{ib} CPE_{op}, CPE_{ib}, W_o and L, where R_s represents solution resistance, the R_{op} and CPE_{op} correspond to the outer layer resistance and Constant phase element (CPE) and R_{ib} and CPE_{ib} are associated with the inner layer resistance and CPE of the PEO, PEO-EPD, and laser textured PEO and PEO-EPD samples. CPE reflects a deviation from the ideal behavior of the double layer capacitance, which is used in the electrochemical circuit instead of a simple capacitor. In addition, L represents the inductance, and W_o describes the Warburg open circuit terminus. The constant phase element defined as the following equation [22], Where Q represents the CPE constant, j is the imaginary number, ω represents the angular frequency (rad per sec), and n is an imperial constant.

$$Z_{CPE} = \frac{1}{Q(j\omega)^n} \tag{5}$$

The PEO, PEO-EPD and laser textured PEO and PEO-EPD coatings comprise of outer porous layer and inner barrier layer characterized by two capacitive loops in their Nyquist plots (Fig. 11). Unlike the PEO, PEO-EPD and laser textured PEO and PEO-EPD samples, the Nyquist plot of the bare substrate showed a single capacitive loop and hence a single layer is considered in the electrical circuit. Substrate shows a single time constant CPE_b with an additional inductive element (L) in the equivalent circuit model, as shown in Fig. 10(a). The R_b and CPE_b are associated with the single layer resistance and CPE of the bare substrate sample. The single capacitive loop of substrate at high frequencies can be related to the porous corrosion product formed on the metal sample, and an inductive loop (R_L-L) at low frequencies attributed to the adsorbed intermediate ions on the surface [39]. The P, PL, PZ and PZL samples exhibited two-time constants (CPE_{op} and CPE_{ib}) indicating a double-layer coating structure (i.e. outer porous layer and inner barrier layer). Besides, the circuit contains Warburg constant (W_o) for P and PZ samples, as shown in Fig. 10(b) whereas PL and PZL sample circuits contain inductance (L) as shown in Fig. 10(c). Nyquist curves of the experimental and fitted results of the fabricated samples P, PL, PZ and PZL along with substrate (S) are shown in Fig. 11. From Fig. 11, it is observed that all samples exhibited different complex plots. In the case of P and PZ samples, Nyquist curves appear as straight lines with a slope of 45°, indicating the presence of diffusion phenomenon along with the charge transfer phenomenon in the corrosion process, which is indicated by the additional W_o constant in the circuit as shown in Fig. 11 [40]. On the other hand, Nyquist curves of PL and PZL samples exhibited complex impedance curves with two loops, and one is the capacitive loop at high frequencies and the other one at low frequencies is the inductive loop attributed to the more adsorption, inhomogeneity, and roughness of the sample surface [1,41]. Thus, the electrical circuit contains additional inductance as shown in Fig. 10.

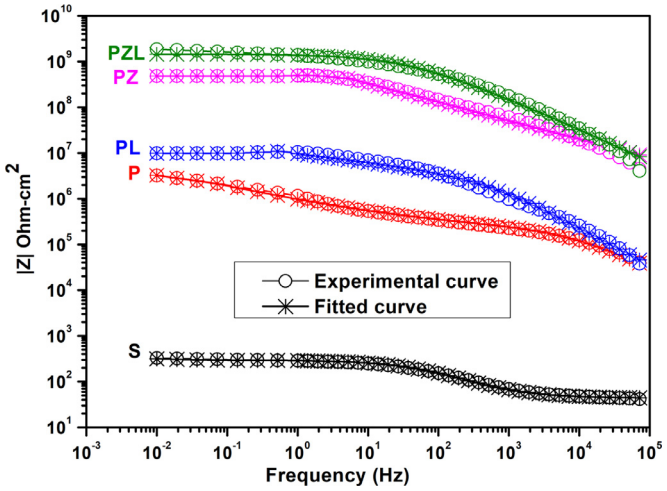

Fig. 12. The Bode impedance plots of the samples substrate (S), P, PL, PZ and PZL samples.

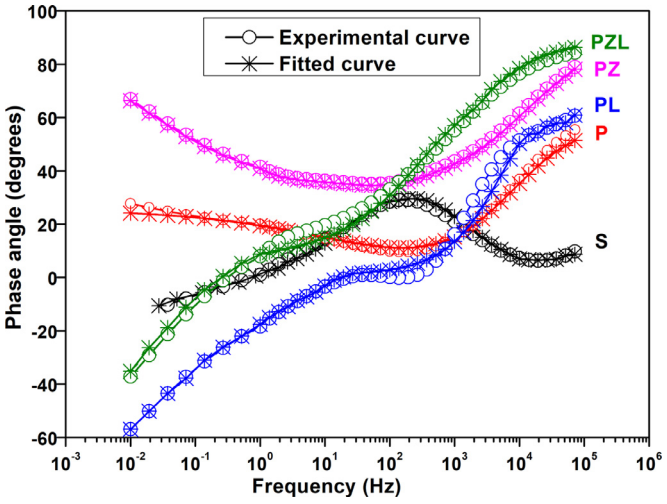

Fig. 13. The Bode phase angle plots of the samples substrate (S), P, PL, PZ and PZL samples.

From Table 6, it is evident that the P, PL, PZ and PZL samples exhibited higher R_{ib} value than the R_{op} value indicating the significance of the inner barrier layer in providing corrosion protection. On the other hand, the CPE_{ib}-T and value CPE_{op}-T of the PZ sample is very low as compared to the P sample indicating a dense inner layer. PL sample showed higher R_{op} value, than that of the P sample, which can be ascribed to the covering of majority of pores and cracks by the molten oxide layer during the laser texturing process. PZ and PZL samples showed higher R_{ib} and R_{op} value than that of P and PL samples specifying its superior anti-corrosion property. It can be noted from EIS measurements, the higher $R_{op} + R_{ib}$ values are obtained for PZ and PZL samples. It is due to the higher thickness and pore-free surface morphology, indicating its higher corrosion resistance than P and PL samples, which is in consonance with the lower current density values reported in Table 5 from PDP analysis.

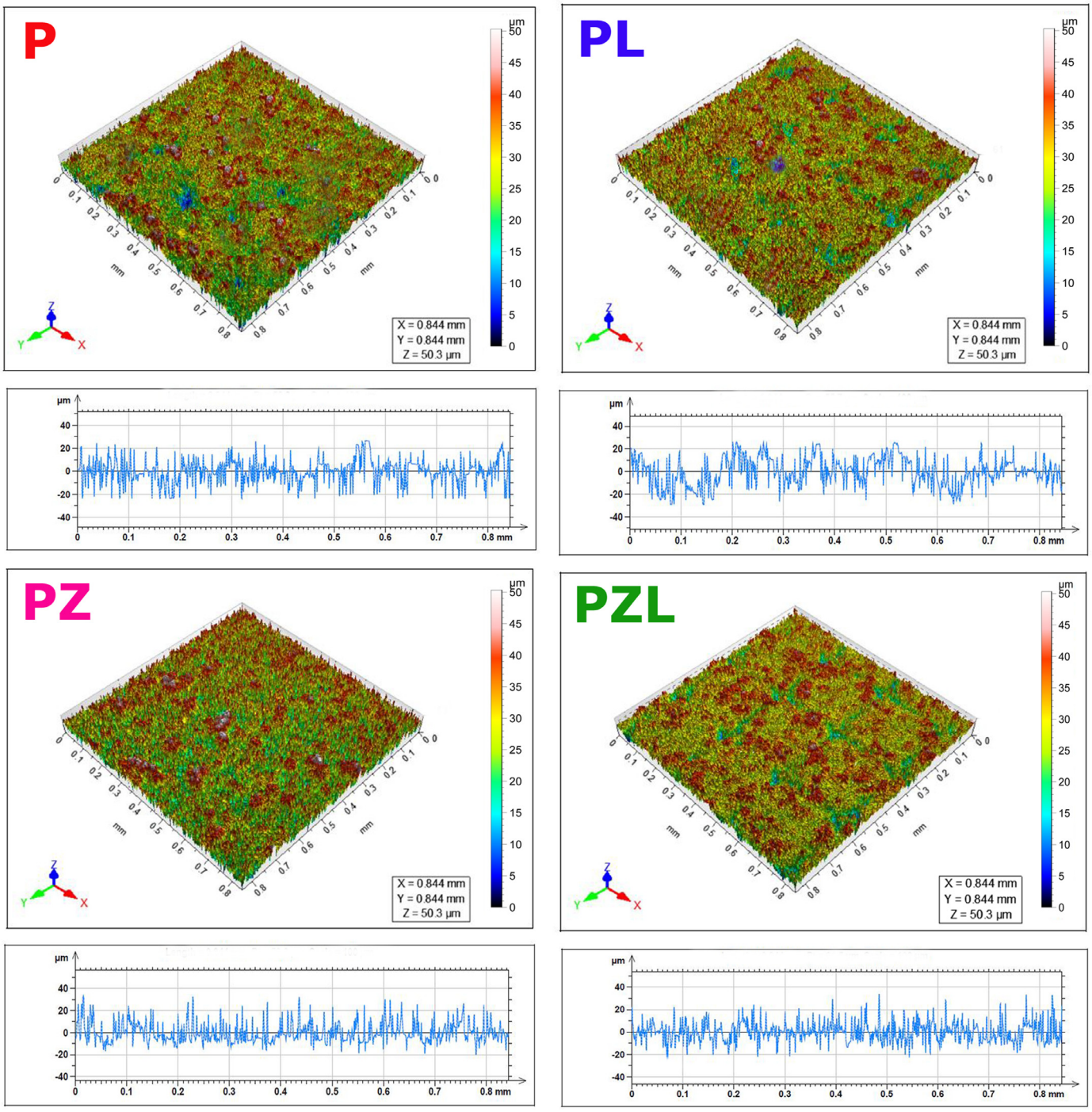

Fig. 14. 3D Surface profile and depth profiles of P, PL, PZ and PZL samples.

Experimental and fitted curves corresponding to the Bode impedance and phase angle plots of the substrate (S), P, PL, PZ and PZL samples, as shown in Figs. 12 and 13. It can be observed that the sample PZ, exhibited higher impedance (10^8 Ω-cm^2) at lower frequency region and higher phase angle at higher frequency region (78°) than the P sample (10^6 Ω-cm^2 and 51°), as shown in Figs. 12 and 13. The higher impedance value at the lower frequencies, along with the higher phase angle at higher frequencies indicates better corrosion resistance corresponding to the relatively pore free morphology and dense coating in the PZ and as well as PZL samples. The PZL sample exhibited a higher impedance of 10^9 order and a higher phase angle of 86°. In accordance with the PDP and EIS results, a laser textured PEO-EPD sample (PZL) exhibited the highest corrosion resistance due to its coating thickness and morphological characteristics.

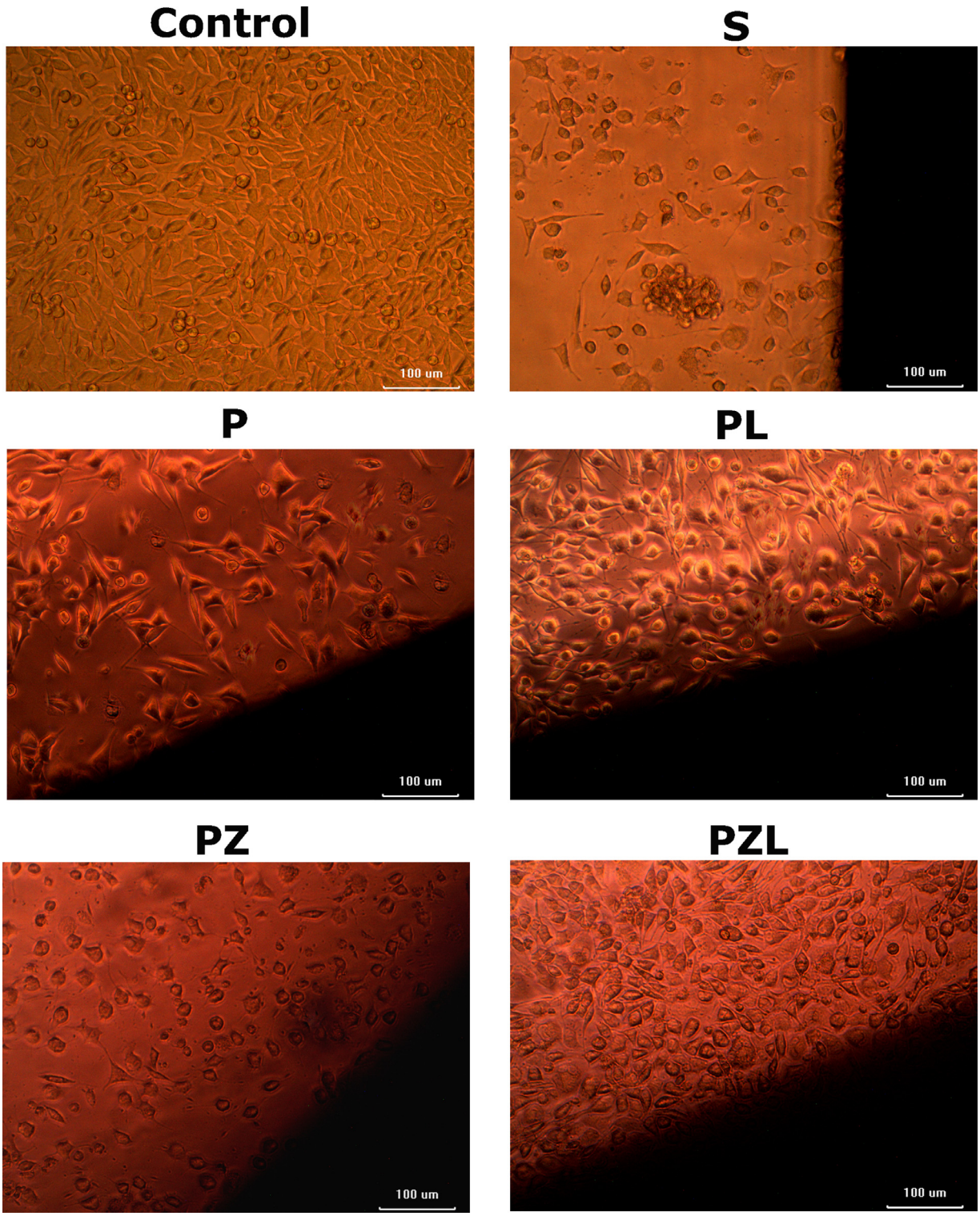

Fig. 15. Phase contrast images showing L-929 mouse fibroblast cells around the substrate (S), P, PL, PZ and PZL samples after 24 h.

3.8. Surface profile analysis

Fig. 14 shows the 3D-profile micrographs and depth profiles of the samples. The average surface roughness parameter values (R_a) of the P, PL, PZ and PZL samples are 1.48± 0.1 μm, 2.51± 0.1 μm, 1.05± 0.1 μm and 2.11± 0.1 μm, respectively. The R_a value of the samples depends on the surface features such as nature of the pores (i.e., deep or shallow pores), microcracks, tracks, grooves and pancake projections [19]. PZ sample showed a lower R_a value than the P sample. It is attributed to the absence of pores in the case of the PZ sample. Arun et al. [42] reported that the addition

of nanoparticles resulted in the reduction of surface porosity due to the closure of the pores by the nanoparticles. On the other hand, laser textured PL and PZL samples showed more hills, pancake projections and grooves compared to the P and PZ samples, which can be attributed to the molten oxide layer spreading along with the laser tracks due to the laser irradiation. 3D optical profile micrograph of the samples corroborated with the FESEM surface morphology of the samples, as shown in Fig. 3. The depth profile of the P, PL, PZ and PZL indicates that the samples have several crests and troughs. The variation in the depth profile of the samples can be attributed to the disparities in the pore size and distribution along with the microcracks and laser tracks. The implant surface with a roughness value between 0.4 μm to 3.5 μm is expected to exhibit a favorable bone response [43]. Therefore, all the coatings are expected to exhibit good response with the adhesion and proliferation of bone cells on the materials, thereby leading to enhanced cell growth in direct contact.

3.9. Direct contact assay

Fig. 15 shows the direct contact assay of L-929 mouse fibroblast cells around the S, P, PL, PZ and PZL samples after 24 h. The morphological changes and growth of the fibroblast cells around the samples were observed by phase contrast microscopy and the morphology and growth of coated samples and untreated substrate were compared. The cell growth at the interface of the samples indicates its non-toxicity and the L-929 cell growth around the coated samples interface appears to be better than the untreated substrate (S). These results indicate that the PEO, PEO-EPD, and laser textured PEO and PEO-EPD samples (P, PZ, PL and PZL) are non-toxic to the cells and provide a favorable environment for the growth of L-929 cells.

4. Conclusions

In this work, Zirconia (ZrO_2) incorporated ceramic coatings were fabricated on the ZM21 Mg alloy by the PEO coupled with EPD process, and subsequently, the PEO and PEO-EPD coating surfaces were modified by the laser texturing process. The major conclusions are as follows.

(i) PEO-EPD coating (PZ sample) showed higher corrosion resistance (i_{corr} $=1.47\times10^{-7}$ mA/cm^2), higher impedance value (of order 10^8) along with the relatively higher phase angle (78°) and higher scratch resistance (L_c=33.28 N), compared to that of PEO coating (P sample).
(ii) The higher corrosion and scratch-resistance of the PEO-EPD coating (PZ sample) was attributed to its higher coating thickness, pore free morphology, reduced roughness and wettability compared to the PEO coating (P sample).
(iii) In comparison with PEO and PEO-EPD coatings, laser surface modified PEO and PEO-EPD coated samples (PL and PZL) exhibited superior corrosion resistance and good wettability. It was attributed due to the ceramic molten oxide layer spreading along with laser tracks and grooves over the sample surface during the laser texturing process.
(iv) Among all the fabricated samples, the PZL sample exhibited a higher corrosion resistance value ($i_{corr}=1.73\times10^{-8}$ mA/cm^2) and higher impedance value (of order 10^9) along with the relatively higher phase angle (86°).
(v) The L-929 cell growth around the P, PL, PZ and PZL samples interface is better than the untreated substrate (S).

By considering the above conclusions, the laser surface modification of the PEO and PEO-EPD coatings can be considered as an optimal technique to attain desired morphological features and enhanced corrosion properties without impeding cell growth.

Declaration of Competing Interest

None.

Acknowledgments

The author (Rameshbabu N) would also like to acknowledge the facilities procured through the grants received from the Science and Engineering Research Board (SERB), New Delhi (SR/S3/ME/0024/2011, dated 3rd July 2012) to carry out this research.

References

[1] Y. Gao, A. Yerokhin, A. Matthews, Surf. Coat. Technol. 234 (2013) 132–142.
[2] P. Tian, D. Xu, X. Liu, Colloids Surf. B 141 (2016) 327–337.
[3] S. Hariprasad, S. Gowtham, S. Arun S, M. Ashok, N. Rameshbabu, J. Alloys Compd. 722 (2017) 698–715.
[4] N. Erdmann, N. Angrisani, J. Reifenrath, A. Lucas, F. Thorey, D. Bormann, Acta Biomater. 7 (2011) 1421–1428.
[5] T.B. Matias, G.H. Asato. G, B.T. Ramasco, W.J. Botta, C.S. Kiminami, C. Bolfarini, J. Mater. Res. Technol. 3 (2014) 203–209.
[6] H.R. Bakhsheshi-Rad, E. Hamzah, A.F. Ismail, M. Aziz, A. Najafinezhad, M. Daroonparvar, J. Alloys Compd. 773 (2019) 180–193.
[7] L.C. Li, J.C. Gao, Y. Wang, Surf. Coat. Technol. 185 (2004) 92–98.
[8] V. Dehnavi, W.J. Binns, J.J. Noel, D.W. Shoesmith, B.L. Luan, J. Magnes. Alloy 6 (2018) 229–237.
[9] G.L. Song, S.Z. Song, Adv. Eng. Mater. 9 (2007) 298–302.
[10] N.E.L. Saris, E. Mervaala, H. Karppanen, J.A. Khawaja, A. Lewenstam, Clin. Chim. Acta 294 (2000) 1–26.
[11] L.Y. Cui, R.C. Zeng, S.K. Guan, W.C. Qi, F. Zhang, S.Q. Li, E.H. Han, J. Alloys Compd. 695 (2017) 2464–2476.
[12] Y.H. Jeong, H.C. Choe, W.A. Brantley, Thin Solid Films 519 (2011) 4668–4675.
[13] M. Jamesh, S. Kumar, T.S.N.S. Narayanan, Corros. Sci. 53 (2011) 645–654.
[14] M. Razavi, M. Fathi, O. Savabi, B.H. Beni, D. Vashaee, L. Tayebi, Ceram. Int. 40 (2014) 9473–9484.
[15] Z.Z. Yin, W.C. Qi, R.C. Zeng, X.B. Chen, C.D. Gu, S.K. Guan, Y.F. Zheng, J. Magnes. Alloy 8 (2020) 42–65.
[16] H. Duan, C. Yan, F. Wang, Electrochim. Acta 52 (2007) 3785–3793.

[17] X. Ma, S. Zhu, L. Wang, C. Ji, C. Ren, S. Guan, J. Alloys Compd. 590 (2014) 247–253.
[18] Y. Chen, Y. Yang, W. Zhang, T. Zhang, F. Wang, J. Alloys Compd. 718 (2017) 92–103.
[19] A. Saikiran, S. Hariprasad, S. Arun, L. Rama Krishna, N. Rameshbabu, Surf. Coat. Technol. 372 (2019) 239–251.
[20] S.S. Farhadi, M. Aliofkhazraei, Gh.Barati Darband, A. Abolhasani, A. Sabour Rouhaghdam, J. Magnes. Alloy 5 (2017) 210–216.
[21] L.Y. Cui, S.D. Gao, P.P. Li, R.C. Zeng, F. Zhang, S.Q. Li, E.H. Han, Corros. Sci. 118 (2017) 84–95.
[22] S. Sarbishei, M.A. Faghihi Sani, M.R. Mohammadi, Ceram. Int. 42 (2016) 8789–8797.
[23] S. Gowtham, S. Hariprasad, T. Arunnellaiappan, N. Rameshbabu, Surf. Coat. Technol. 313 (2017) 263–273.
[24] A. Riveiro, R. Soto, J. del Val, R. Comesana, M. Boutinguiza, F. Quintero, F. Lusquinos, J. Pou, Appl. Surf. Sci. 302 (2014) 236–242.
[25] M. Hashim, K.E.S. Raghavendra Babu, M. Duraiselvam, N. Harshad, Mater. Des. 46 (2013) 546–551.
[26] J. Li, S. Zhao, F. Du, Y. Zhou, H. Yu, J. Alloys Compd. 739 (2018) 489–498.
[27] M. Ji, J. Xu, M. Chen, M. El. Mansori, Ceram. Int. 46 (2020) 7161–7169.
[28] K.M. Lecka, J. Gasiorek, A.M. Nowacka, B. Szczygieł, A.J. Antończak, Surf. Coat. Technol. 366 (2019) 179–189.
[29] T. Kokubo, H. Takadama, Biomaterials 27 (2006) 2907–2915.
[30] R.F. Zhang, S.F. Zhang, Corros. Sci. 51 (2009) 2820–2825.
[31] S. Hariprasad, M. Ashfaq, T. Arunnellaiappan, Manu Harilal, N. Rameshbabu N, Surf. Coat. Technol. 292 (2016) 20–29.
[32] R.F. Zhang, S.F. Zhang, J.H. Xiang, L.H. Zhang, Y.Q. Zhang, S.B. Guo, Surf. Coat. Technol. 206 (2012) 5072–5079.
[33] K.M. Lee, B.U. Lee, S.I. Yoon, E.S. Lee, B. Yoo, D.H. Shin, Electrochim. Acta 67 (2012) 6–11.
[34] R. Arrabal, E. Matykina, P. Skeldon, G.E. Thompson, J. Mater. Sci. 43 (2008) 1532–1538.
[35] T. Arunnellaiappan, M. Ashfaq, L. RamaKrishna, N. Rameshbabu, Ceram. Int. 42 (2016) 5897–5905.
[36] G. Liu, K. Du, K. Wang, Appl. Surf. Sci. 388 (2016) 313–320.
[37] T. Nishimura, Y. Ogino, Y. Ayukawa, K. Koyano, Dent. Mater. J. 37 (2018) 650–658.
[38] L. Zhang, E.A.A. Mohammed, A. Adriaens, Surf. Coat. Technol. 307 (2016) 56–64.
[39] R. Aliramezani, K. Raeissi, Monica Santamaria, Amin Hakimizad, Surf. Coat. Technol. 329 (2017) 250–261.
[40] K. Venkateswarlu, N. Rameshbabu, D. Sreekanth, A.C. Bose, V. Muthupandi, N.K. Babu, S. Subramanian, Appl. Surf. Sci. 258 (2012) 6853–6863.
[41] S. Wang, Y. Xia, L. Liu, N. Sia, Ceram. Int. 40 (2014) 93–99.
[42] S. Arun, T. Arunnellaiappan, N. Rameshbabu, Surf. Coat. Technol. 305 (2016) 264–273.
[43] C. Wei, W.J. Pan, M.S. Hung, Surf. Coat. Technol. 224 (2013) 8–17.